Anomalous scaling and intermittency in three-dimensional synthetic turbulence

Carlos Rosales*
Department of Mechanics, Technical University Federico Santa Maria, Av. España 1680, Valparaiso, Chile

Charles Meneveau†
Department of Mechanical Engineering and Center for Environmental and Applied Fluid Mechanics, The Johns Hopkins University, 3400 North Charles Street, Baltimore, Maryland 21218, USA

(Received 19 February 2008; revised manuscript received 7 June 2008; published 23 July 2008)

A simple method, the multiscale minimal Lagrangian map (MMLM) approach, to generate synthetic turbulent vector fields was previously introduced [C. Rosales and C. Meneveau, Phys. Fluids **18**, 075104 (2006)]. It was shown that the synthesized fields reproduce many statistical and geometric properties observed in real, isotropic, turbulence. In this paper we investigate if this procedure, which applies a minimal Lagrangian map to deform an initial Gaussian field, can produce also anomalous scaling in the inertial range. It is found that the advection Lagrangian map time scale is crucial in determining anomalous scaling properties. With the sweeping time scale used in the MMLM approach, non-Gaussian statistics and realistic geometric features are reproduced at each scale, but anomalous exponents are not observed; i.e., we observe nearly 1941 Kolmogorov scaling. Conversely, if the appropriate Kolmogorov inertial-range turnover time scale is used in a modified approach [the multiscale turnover Lagrangian map (MTLM) method], fields with realistic anomalous scaling exponents are reproduced. Remarkably, the intermittency and multifractal nature of the energy dissipation is also found to be quite realistic. Finally, the properties of the pressure field derived from the MTLM velocity field are studied and found to be quite realistic also. The results shed new light on what are minimal dynamical requirements for the generation of anomalous scaling and intermittency in turbulent flow: at least one turnover time for small eddies to be sufficiently deformed, as well as the accumulation of spatially correlated deformations across scales.

DOI: 10.1103/PhysRevE.78.016313 PACS number(s): 47.27.−i, 47.27.E−, 47.11.St, 47.53.+n

I. INTRODUCTION

By synthetic turbulence one generally means the construction of field variables (such as velocity distributions) having characteristic features of turbulent fluctuations, but that can be obtained at a reduced computational cost in comparison with a formal numerical solution of the full Navier-Stokes equations. In this sense, different methods to produce synthetic turbulence substitute, to greater or lesser extent, the true turbulence dynamics by simpler processes aimed to reproduce observable characteristics. Besides its practical applications in numerical simulation of turbulent flows, such as for generating initial and inflow boundary conditions, synthetic turbulence is also of interest to further understanding fundamental properties of turbulent motion. In particular, finding the most reduced set of processes that still allow the manifestation of intrinsic properties of turbulence helps in understanding turbulence physics and its universal aspects. Prior works on generating synthetic turbulence have emphasized different aspects of turbulence, such as fundamental scaling properties through wavelet-based or multiplicative approaches [1–5] and synthetic turbulence to evaluate subgrid-scale stresses or mixing of scalars [6–9], as well as kinematic models to study turbulent dispersion [10,11]. A framework for vector-valued multifractal measures was established in Ref. [12], which has been applied in the construction of vector-valued self-similar random fields [13].

In Ref. [14] a new procedure to generate three-dimensional (3D) non-Gaussian synthetic turbulent vector fields was introduced. The procedure is based on the minimal Lagrangian map, by which an initial Gaussian field generated using random-phase Fourier modes is deformed. The deformation takes place by moving fluid particles of a sequence of low-pass filtered fields at their fixed velocity for some scale-dependent time interval. At any scale, when noninteracting fluid parcels are considered, the equation of motion reduces to the Riemann equation

$$\partial_t \mathbf{u} + (\mathbf{u}\cdot\nabla)\mathbf{u} = 0, \tag{1}$$

corresponding to a system of particles each moving with constant velocity in Lagrangian coordinates. The solution is $\mathbf{u}(\mathbf{x}'(t),t)=\mathbf{u}(\mathbf{x},\mathbf{0})$ where $\mathbf{x}'(t)$ is the Lagrangian position of the particle ascribed at $t=0$ to the Eulerian point $\mathbf{x}$—i.e.,

$$\mathbf{x}'(t) = \mathbf{x} + t\mathbf{u}(\mathbf{x},0). \tag{2}$$

This map has been called the "naive Lagrangian map" in Refs. [15,16] and was called the "minimal Lagrangian map" in Ref. [14]. It is equivalent to the inviscid 3D Burgers equation until the appearance of the first shock [15–19]. It also has been used in the study of nonlinear formation of large-scale structures in cosmology [17,18]. In practice, after discrete particles have been moved at constant velocity for some time interval to new positions, the procedure [14] then includes an interpolation step to reexpress the velocities on a regular grid, and then the divergence-free condition is imposed by projection in wave-number space. The mapping is

*carlos.rosales@usm.cl
†meneveau@jhu.edu

applied in a multiscale fashion, with a scale-dependent time interval, and acting on velocity fields which have been low-pass-filtered over a sequence of scales. More details about the construction procedure are given in Sec. II.

It was shown in Ref. [14] that this simple procedure, called the multiscale minimal Lagrangian map (MMLM) approach, can reproduce many fundamental trends of turbulence, such as the skewness and flatness of velocity derivatives, the general form of probability density functions (PDF) for velocity derivatives and velocity increments, the joint PDF of second and third invariants of the velocity gradient tensor, the preferential alignment of vorticity with the intermediate eigenvector of the strain-rate tensor, and other statistical characteristics of enstrophy and strain-rate production in the strain-dominated regions of the field.

In Ref. [14] it was also observed that the PDFs of resulting velocity increments depended on scale, with near Gaussian statistics at large scales and elongated non-Gaussian tails for small displacements. As a consequence, the fields displayed increasing flatness towards small scales, which is an indication of intermittency. Inertial-range intermittency is an important topic in the modern theory of turbulence since it represents a departure from the statistical scale invariance in that range, which is implicit in the 1941 Kolmogorov theory. A fundamental result in homogeneous isotropic turbulence is Kolmogorov's four-fifths law, for the longitudinal third order structure function [20],

$$\langle [\delta u_{\parallel}(r)]^3 \rangle = -\frac{4}{5}\varepsilon r, \tag{3}$$

where $\delta u_{\parallel}(r) \equiv [\mathbf{u}(\mathbf{x}+\mathbf{r})-\mathbf{u}(\mathbf{x})]\cdot \mathbf{r}/r$ is the longitudinal velocity increment over a separation vector $\mathbf{r}$ and ε is the mean energy dissipation rate. A dimensional generalization of this result leads to a scaling for the pth-order longitudinal structure functions in the form

$$\langle [\delta u_{\parallel}(r)]^p \rangle \propto r^{\zeta_p}, \tag{4}$$

with $\zeta_p = p/3$, when the velocity field possess the scale invariance of (1941) Kolmogorov theory. Much experimental and numerical evidence has accumulated that shows that intermittency and anomalous scaling in the inertial range occurs in turbulent flows (see, e.g., [21,22] and references therein). This is manifested by the deviation of the measured scaling exponents ζ_p from the $p/3$ value predicted for the nonintermittent case and ζ_p becoming a nonlinear function of the order p. However, the synthetic fields generated and analyzed in Ref. [14] did not cover an extended inertial range, so that the observed behavior could not be used to measure ζ_p or to assess possibly anomalous inertial-range scaling. An important question that arises then is whether such a simple procedure can produce also realistic anomalous scaling in the inertial range. One of the objectives of this paper is to address this question.

The systematic change in the statistics of $\delta u_{\parallel}(\mathbf{r})$ in the inertial range is believed to be associated with the energy cascade process. The turbulence intensity at large scales varies randomly with position, while the interaction among them leads to the random formation of smaller scales within the larger ones. Inside these small scales, yet smaller scales are produced by similar mechanisms, and so on until reaching the dissipative scales. In this way the spatial distribution of turbulence intensity at a given scale preconditions that of smaller scales in the same spatial region. Zones of higher intensity will tend to have a higher energy flux rate to smaller scales originating from them, and consequently the resulting smaller scales at these particular locations will be more active, preconditioning in turn the next generation of scales. As a result, the effects of turbulence intensity concentration introduced at each stage of the cascade are superposed, leading to a cumulative deformation of the statistical distribution of $\delta u_{\parallel}(\mathbf{r})$, so that rare events of atypically strong fluctuations become more frequent as the scale is reduced. Although this scenario is based on several phenomenological statements, it is believed to provide a qualitatively correct description of the physical process involved. The dissipation field also is known to be highly intermittent in turbulent flows [21,23,24], with anomalous scaling observed as function of coarse-graining scale. Other important turbulence variables that are associated with the Lagrangian fluid accelerations and are also related to intermittency are pressure fluctuations, pressure increments, and pressure gradients.

Most of the methods that seek to introduce intermittency in synthetic turbulence are inspired by the ideas of the previous paragraph and employ some form of scale-by-scale multiplicative construction to mimic this cascading process with cumulative distortive action. These multiplicative constructions usually proceed by distributing an appropriate measure contained in a whole one-dimensional interval, over disjoint subintervals. The ratio of the measure inherited by an offspring subinterval to the measure contained in the parent interval is determined by a multiplier which is taken from a given probability distribution, or is a fixed parameter (Refs. [1,3,25]). In a model introduced by Juneja *et al.* [4], the synthetic velocity field is a superposition of skewed tent functions of different scales, locations, and amplitudes. The scales are chosen randomly from a distribution analogous to the hierarchy of scales in a cascade process, and the amplitudes are proportional to a measure distributed by a multiplicative construction. In order to introduce skewness and other nonzero odd-order structure functions, the tent functions include a skew parameter, which is adjusted such that the synthetic turbulence signal is consistent with Kolmogorov's four-fifths law. In the MMLM method [14] no attempt is made to introduce intermittency by an *a priori* statistical model and nor are there separate parameters to be tuned to reproduce some prescribed anomalous scaling exponents. The spatial concentration of intense turbulent activity stems essentially from the action of the advective term in the Navier-Stokes equation (which is represented by the displacement of the fluid particles by their own constant initial velocity). The ability of just the advective term to generate intermittency in the sense of long tails in the PDFs is reasonably well understood [26–29]. Nevertheless, the issue of anomalous scaling is more subtle. Hence, it is of interest to determine if inertial-range anomalous scaling arises even in the simple dynamics on which the MMLM approach is based.

In Sec. II we review the MMLM approach and structure functions up to 12th order for the synthetic velocity field are

obtained and analyzed in Sec. III as function of the time scale used in the advection step at each scale. Based on the results and observations about the effects of imposed time scale, a modified procedure is introduced in Sec. IV which is based on the scale-dependent turnover time. Using such a more physically relevant time scale is shown to yield synthetic fields that accurately reproduce anomalous scaling exponents. Some features of the vorticity field are studied in Sec. V, and Sec. VI presents an analysis of the multifractal characteristics of the energy dissipation. Finally Sec. VII documents statistical properties of the pressure field associated with the synthetic velocity fields generated.

II. BACKGROUND

The MMLM approach begins with a standard Gaussian divergence-free velocity field constructed by superposing random-phase Fourier modes and a prescribed energy spectrum. At this starting point the method is equivalent to what is commonly used to initialize simulations of isotropic turbulence in Fourier space [30,31]. The basic idea of the MMLM approach is based first on a multiscale decomposition at any arbitrary level n or scale $\ell_n = 2^{-n}\mathcal{L}$, $n=1,\ldots,M$ (where $\mathcal{L}$ is a reference large-scale that typically scales with the turbulence integral scale):

$$\mathbf{u} = \mathbf{u}_n^< + \mathbf{u}_n^>. \tag{5}$$

The decomposition used in Ref. [14] is based on sharp filtering in Fourier space at cutoff wave number $k_{c,n} = \pi/\ell_n$. The filtered field $\mathbf{u}_n^<$ is obtained by low-pass-filtering the velocity field generated using the MMLM method in the previous level $n-1$, except for the first step when $n=1$, for which the initial random field is filtered. At each scale, the field is sampled in physical space on a grid that uses the correspondingly coarse mesh spacing ℓ_n. The MMLM method begins at the largest scale available (lowest $n=1$). The MMLM method is based on distorting the large-scale portion of such a field by mapping fluid particles from their given positions $\mathbf{x}$ (grid points with mesh spacing ℓ_n) to new positions $\mathbf{x}'$ determined by their Lagrangian displacements:

$$\mathbf{x}' = \mathbf{x} + t_n \mathbf{u}_n^<(\mathbf{x}), \quad \mathbf{v}_n^<(\mathbf{x}') \equiv \mathbf{u}_n^<(\mathbf{x}). \tag{6}$$

The time interval t_n is determined as

$$t_n = \frac{\ell_n}{u_{\mathrm{rms},n}^<}, \tag{7}$$

where $u_{\mathrm{rms},n}^<$ is the root-mean-square (rms) characteristic velocity of the velocity field low-pass filtered at scale ℓ_n. Note that using this sort of Courant-Friedricks-Lewey (CFL) time scale allows particles to remain within a region whose size is (in an rms sense) on the order of the mesh size ℓ_n. Allowing much longer times than this was shown in Ref. [14] to lead to resulting velocity increments with Gaussian statistics, due to mixing of particles that could originate from parts of the flow with uncorrelated initial velocities. Conversely, using much smaller times, the deformation was insufficient and did not lead to significant non-Gaussianity. New velocities $\mathbf{v}_n^<(\mathbf{x})$ at the Eulerian positions $\mathbf{x}$ are obtained from the deformed velocity field (residing on the nonuniform, deformed mesh) by interpolating over the velocities of nearby surrounding fluid particles that have arrived close to $\mathbf{x}$ after being moved by Eq. (6). The interpolation used is a simple weighted average, using the inverse of the distance $|\mathbf{x}-\mathbf{x}'|$ as a weighting function, over a ball of radius ℓ_n around $\mathbf{x}$:

$$\mathbf{v}_n^<(\mathbf{x}) = \sum_{|\mathbf{x}-\mathbf{x}'|<\ell_n} |\mathbf{x}-\mathbf{x}'|^{-1} \mathbf{v}_n^<(\mathbf{x}') \Big/ \sum_{|\mathbf{x}-\mathbf{x}'|<\ell_n} |\mathbf{x}-\mathbf{x}'|^{-1}. \tag{8}$$

The new velocity field $\mathbf{v}_n^<$ is made solenoidal by projecting it onto its divergence-free part. This is done in wavenumber space, yielding

$$\hat{\mathbf{w}}_n^<(\mathbf{k}) = \mathbf{P}(\mathbf{k}) \cdot \hat{\mathbf{v}}_n^<(\mathbf{k}). \tag{9}$$

Here, $\mathbf{P}(\mathbf{k})$ stands for the projection tensor $(P_{ij} = \delta_{ij} - k_i k_j / k^2)$ and $\hat{\cdot}$ denotes Fourier-transformed quantities. This projection could be regarded as an explicit addition of a pressurelike effect that enforces zero divergence, although this is a purely numerical action, without any dynamical connection with Eq. (1).

Also the amplitudes of the Fourier modes $\hat{\mathbf{w}}_n^<$ are rescaled in order to match a prescribed energy spectrum $E(k)$ according to

$$\hat{\mathbf{z}}_n^<(\mathbf{k}) = \hat{\mathbf{w}}_n^<(\mathbf{k}) \left[\frac{E(k)}{\frac{1}{2} \sum_{|\mathbf{q}|=k} \hat{\mathbf{w}}_n^<(\mathbf{q}) \cdot \hat{\mathbf{w}}_n^{<*}(\mathbf{q})} \right]^{1/2}. \tag{10}$$

This divergence-free field at large scales is now combined with the high-pass-filtered part of the velocity field, $\mathbf{u}_n^>$, which has remained unaltered at the current level:

$$\mathbf{u} = \mathbf{z}_n^< + \mathbf{u}_n^>. \tag{11}$$

Then the field $\mathbf{u}$ is taken as the starting point to advance to the next level. For this purpose it is filtered again, now at a higher cutoff wave number for level $n+1$, and the mapping given by Eqs. (6) and (7) and the other operations are applied once more with $n \leftarrow n+1$. In this way the distortive action advances from a scale of the order of the integral scale L toward progressively smaller scales, until reaching a scale of the order of Kolmogorov scale η. At the end of this process, the effects of the mappings have been superposed and accumulated over a range of spatial scales. More details can be found in Ref. [14].

III. STRUCTURE FUNCTIONS FOR THE MMLM FIELD

First, the MMLM approach outlined in the previous section was used to generate synthetic velocity fields over a regular mesh of $N_M^3 = 512^3$ points in a domain of size $(2\pi)^3$ with periodic boundaries. The smallest scale considered is given by the separation $\ell_M = 2\pi/N_M$ between neighboring points in this mesh, while larger scales are represented by reduced numbers of points, $N_n = N_M/2^{M-n}$, for each level $n = 1,\ldots,M$ in the sequence. The starting Gaussian velocity field is generated as Fourier modes with random phases, and the prescribed energy spectrum is [32]

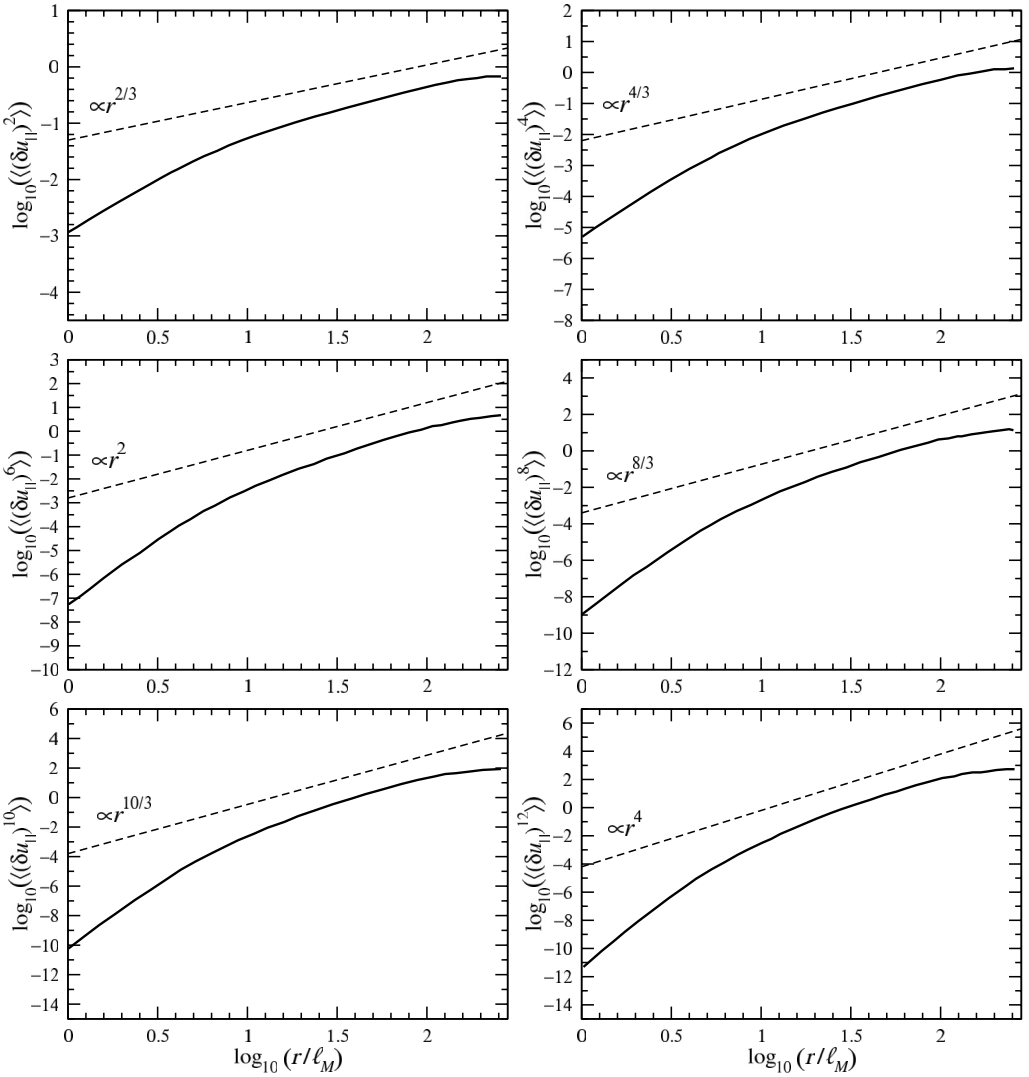

FIG. 1. Longitudinal velocity structure functions for a 512^3 MMLM field. Separation r is nondimensionalized by the smallest scale ℓ_M. The dashed lines correspond to the slope for Kolmogorov scaling as indicated.

$$E(k) = C\varepsilon^{2/3}k^{-5/3}\exp\{-\beta\,[(k\eta)^4 + c_\eta^4]^{1/4} - c_\eta]\}, \quad (12)$$

with $C=1.5$, $\beta=5.2$, and $c_\eta=0.4$. The spectrum (12) does not include an energy-containing range, so that the extension of the inertial range is increased for the given grid resolution. The parameters $u_{\rm rms}$, ε, and the viscosity ν were specified such that the Reynolds number (at Taylor scale) is $\mathrm{Re}_\lambda = 200$ and $k_{\max}\eta = 2.1$. The MMLM procedure is applied starting at $n=1$ with a coarse grid with $N_1^3 = 16^3$ modes—i.e., in this case $\mathcal{L} = 2\pi/8$. The sequence is applied recursively for $16^3 \triangleright 32^3 \triangleright 64^3 \triangleright 128^3 \triangleright 256^3 \triangleright 512^3$—i.e., $M=6$. The resulting field is analyzed focusing on various statistical commonly used to quantify intermittency and local structure in turbulence. First, all of the observations made in [14] for a 256^3 field are reproduced for the present 512^3 field, such as the skewness of longitudinal and flatness of transverse, velocity derivatives, elongated tails in the PDFs for velocity derivatives and velocity increments, the preferential alignment of vorticity with the intermediate eigenvector of the strain-rate tensor, the prevalence of axisymmetric extension, and the tear-shaped joint PDFs of second and third invariants of the velocity gradient tensor.

Here the interest is in scaling properties of the structure functions. Figure 1 (solid lines) shows the structure functions of various orders. The structure functions tend towards an approximated power-law behavior, but only over a limited range of lengths r corresponding approximately to an interval of $17\ell_M < r < 100\ell_M$, which corresponds approximately to $25\eta < r < 150\eta$ since $\ell_M = 1.5\eta$.

For the region where the slopes remain approximately constant, those slopes fall very near the Kolmogorov scaling (K41 slopes are indicated by the dashed lines). In order to check whether this scaling behavior changes as function of available scale ratio ("Reynolds number") the procedure is repeated for a domain using 1024^3 points, again starting the sequence with an ensemble of 16^3 points, but proceeding until $M=7$. For this case the parameters were set such that $\mathrm{Re}_\lambda = 476$ and $k_{\max}\eta \approx 1$. Results are presented in Fig. 2 as the solid lines. For better visualization, the ranges of scales

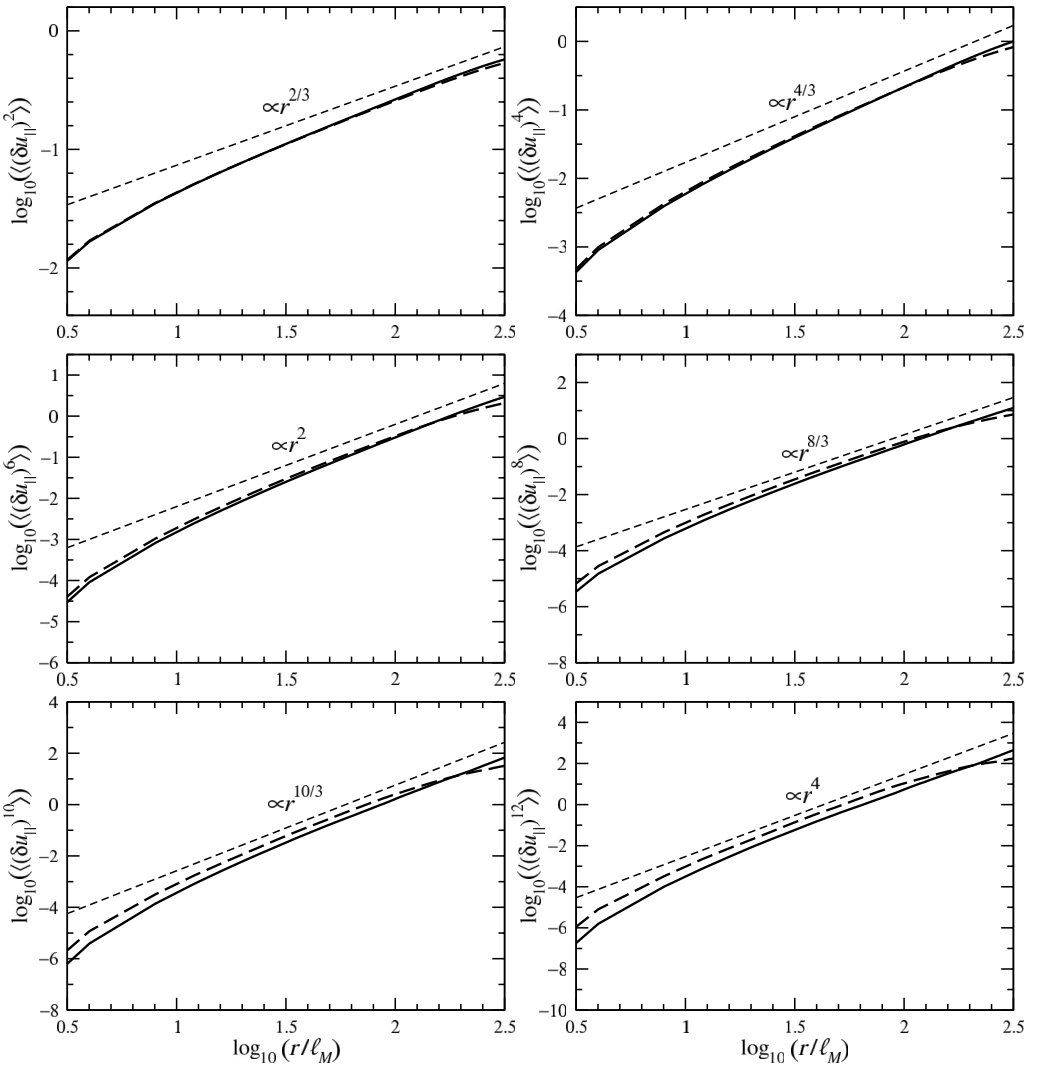

FIG. 2. Longitudinal velocity structure functions for 1024^3 MMLM fields. Separation r is nondimensionalized by the smallest scale ℓ_M. Solid lines: using the spectrum function (12). Dashed lines: using the spectrum function (13). The thin short-dashed lines correspond to the slope for Kolmogorov scaling as indicated.

with $\log_{10}(r/\ell_M)$ below 0.5 and above 2.5 have been excluded, since the former is well into the dissipative range and the latter contains large-scale inhomogeneities. These plots show slightly better power-law behavior still with scaling exponents that do not differ significantly from the values predicted by (1941) Kolmogorov theory. Recall that these synthetic fields still exhibit all of the turbulent features mentioned before (such as skewness and PDFs for velocity gradients, statistics for enstrophy and strain-rate production, vorticity alignment, etc.). However, quite clearly there is no anomalous scaling behavior.

The large-scale energy-containing portion of the spectrum is not included in function (12) in order to extend as much as possible the inertial range. To discard the possibility that the observed behavior is somehow associated with a lack of realistic turbulent characteristics at the largest scales at which the procedure starts, we compute another case with a spectrum that contains a realistic large-scale portion [32]

$$E(k) = C\varepsilon^{2/3}k^{-5/3}\left[\frac{kL}{((kL)^2 + c_L)^{1/2}}\right]^{5/3+p_0} \times \exp\{-\beta\,[(k\eta)^4 + c_\eta^4]^{1/4} - c_\eta]\}, \tag{13}$$

where p_0 is taken to be 4 and c_L is determined so that $E(k)$ integrates to the prescribed total kinetic energy $3/2u_{\mathrm{rms}}^2$. This case has an equivalent Reynolds number of $\mathrm{Re}_\lambda = 407$ and $k_{\max}\eta \approx 1$, and the sequence starts from an ensemble of 8^3 points, advancing up to the 1024^3-point level (i.e., $M=8$). Structure function results for this field are shown by the thick dashed lines in Fig. 2. As expected, the approximate power-law scaling range is narrower now, due to the shortened inertial range, but still the scaling exponents are quite close to K41 behavior and there is no indication of anomalous scaling. Figure 3 shows the modification of the 12th-order structure function at each step in the MMLM sequence for this second case. The lower solid line corresponds to the initial Gaussian field, while the upper solid line is the final result,

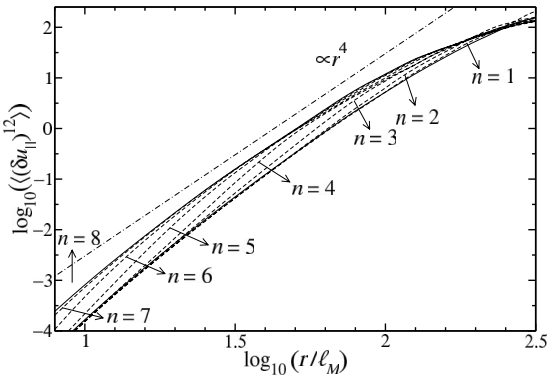

FIG. 3. Twelfth-order longitudinal structure function for the 1024^3 MMLM field with spectrum (12), at different stages in the sequence $n=1,\ldots,M$. Lower solid line corresponds to the initial Gaussian field; upper solid line is the final result; results at intermediate levels n are shown with dashed lines.

after applying the procedure to the last level ($n=8$) in the sequence. The range for $\log_{10}(r/\ell_M)<0.9$ is not shown in this plot, as in the previous figure one can see that an approximate inertial range ends at $\log_{10}(r/\ell_M)\approx 1$. The results at intermediate levels are shown with dashed lines. It can be seen that as the sequence progresses, a narrow interval is forming around $\log_{10}(r/\ell_M)\approx 2$ in which the slope of the curve is depressed. However, the total cumulative effect is weak at smaller scales and the final curve bends down toward a slope not very different of the slope corresponding to Kolmogorov scaling.

The parameter t_n is the most important quantity that determines the extent of the distortion at each scale introduced by the Lagrangian mapping. As given by Eq. (7), t_n is equivalent to the average time that it takes for a typical particle to move between neighboring nodes (sweeping time scale [33]). As said before, this allows enough distortion to give rise to non-Gaussian turbulent features, but avoiding a rerandomization of the field by the combination of uncorrelated velocities. This choice of t_n, however, depends on an arbitrary length (ℓ_n) not connected with the intrinsic dynamics of the turbulence. A more physically relevant time scale is the turbulent Lagrangian "eddy turnover" time proper of that length scale. Therefore, it is possible that the lack of anomalous scaling could be related with the disparity between these two time scales. Indeed, initial tests where the degree of distortion was increased by doubling the value of t_n at each level showed a more significative bending to lower slopes in the log-log curves of the structure functions at large scales, while the rest of the scaling range remained basically unmodified. This motivates us to consider a modified procedure in which the Lagrangian map occurs over a more physically motivated time scale.

IV. MULTISCALE TURNOVER LAGRANGIAN MAP PROCEDURE

The characteristic "turnover" time at scale r (or eddy turnover time) in a turbulent flow can be estimated as

$$\tau_r \sim \frac{r}{\delta u_r}, \tag{14}$$

where δu_r is a typical value for the relative velocities associated to that scale. It is well known that in the phenomenology of turbulence the average energy flux through scale r in the inertial range is considered constant and equal to the dissipation rate ε, leading to the relation $\delta u_r \sim (r\varepsilon)^{1/3}$. Taking as scale r the neighboring points separation ℓ_n of the nth level, we have

$$\tau_n \sim \frac{\ell_n^{2/3}}{\varepsilon^{1/3}}. \tag{15}$$

On the other hand, since the mapping is done using a low-pass velocity field, the rms velocity $u_{\mathrm{rms},n}$ entering into the calculation of t_n is approximately equal to the rms velocity u_{rms} of the whole turbulent field that we are trying to mimic, for a typical spectrum where the energy is mostly contained at large scales. Since $u_{\mathrm{rms}} \sim (\varepsilon L)^{1/3}$, the ratio of t_n to the turnover time can be estimated as

$$\frac{t_n}{\tau_n} \approx \left(\frac{\ell_n}{L}\right)^{1/3}. \tag{16}$$

τ_n is regarded as representative of the time taken for a structure of size r to experience a considerable distortion by the turbulent motions and to pass its energy on to yet smaller scales via the cascade. Relation (16) shows that t_n is progressively smaller in proportion to τ_n as the procedure advances from one level to the next one, so that there is an increasing disparity between t_n and the characteristic "turnover" time of true turbulence for the particular scale at which the mapping with t_n is being applied.

Hence, the mapping procedure will be modified such that the particles will be advanced for an accumulated equivalent time τ_n given by Eq. (15) at each level, instead of t_n. It was established in Ref. [14] that the particle displacements should not be very different from the original separation ℓ_n. In this way, regions of steep velocity gradients are generated mostly by converging trajectories of particles whose initial separation was of the order of ℓ_n and, therefore, had correlated velocities (since the field was filtered in order to be smooth at scale ℓ_n). For larger displacements, the decorrelation among the velocities of arriving particles leads to a rerandomization of the velocity field, destroying the coherency introduced by the mapping at the preceding level. Because of this, the total advancement will be executed in several steps at each level, so that the rms displacement in one step is still of the order of ℓ_n. More precisely, for each level in the hierarchy of scales, the sequence of mapping (6), interpolation and projection is applied D times, with

$$D = \left[\frac{u_{\mathrm{rms},n}}{(\ell_n\varepsilon)^{1/3}}\right] \tag{17}$$

($[\cdot]$ denotes nearest integer), and each t_n to be used in Eq. (6) is given by the corresponding fraction of τ_n—namely,

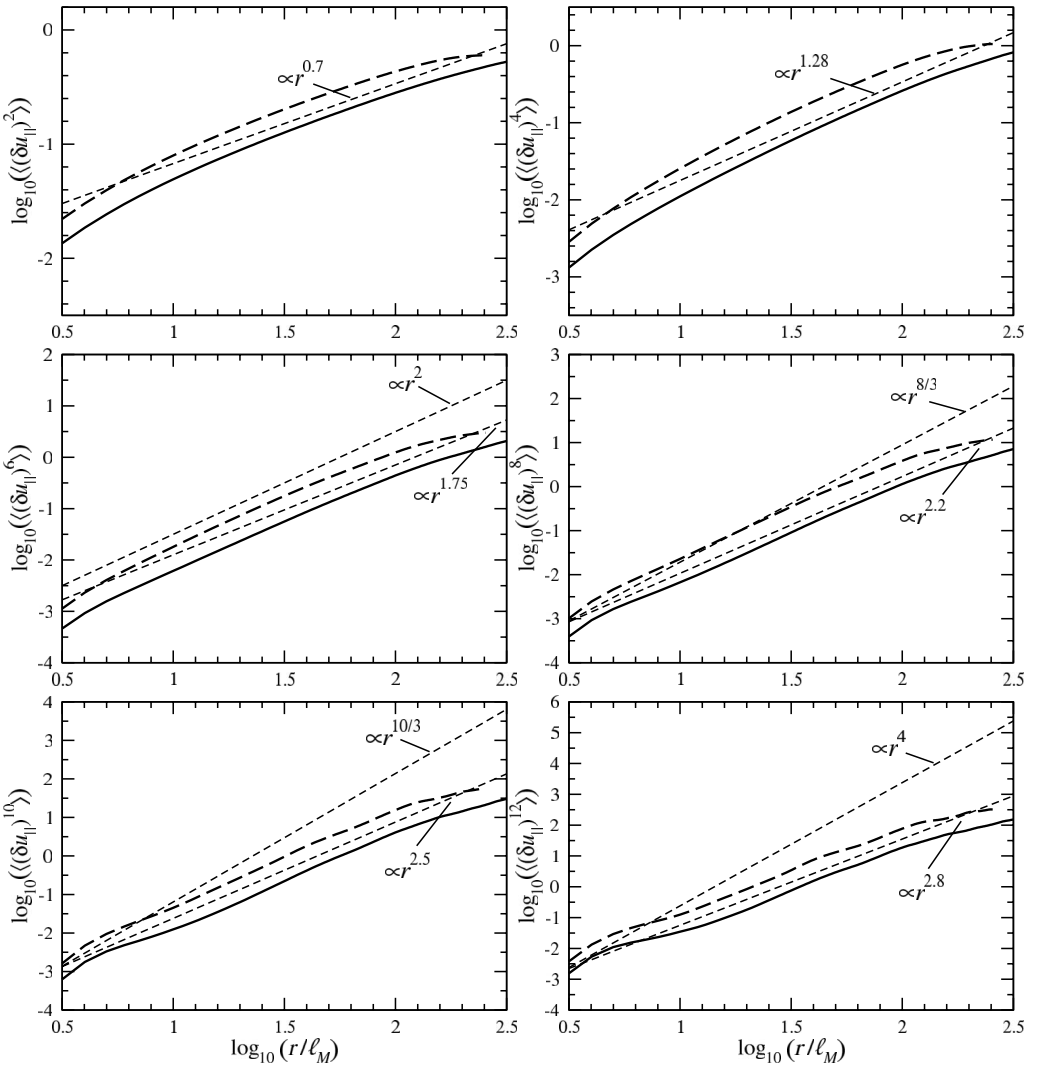

FIG. 4. Longitudinal velocity structure functions for 1024^3 (solid lines) and 512^3 (dashed lines) MTLM fields. Separation r is nondimensionalized by the smallest scale ℓ_M. The thin dashed lines correspond to the power laws as indicated.

$$t_n = \frac{1}{D}\left(\frac{\ell_n^2}{\varepsilon}\right)^{1/3}. \tag{18}$$

By repeating the procedure D times, a total time τ_n can be accumulated through a sequence of D time steps, each of duration equal to t_n. After each of these advancements, the interpolation to obtain the velocities $\mathbf{v}_n^<$ at the Eulerian points $\mathbf{x}_n$ is applied. These velocities are rescaled directly in physical space to keep constant the rms velocity of the field, and the projection onto a divergence-free condition is performed. For brevity, this modified mapping procedure will be denoted as the multiscale turnover Lagrangian map (MTLM) in the following.

A new 1024^3-point synthetic turbulent field was generated with the MTLM approach. The prescribed energy spectrum has the form given by Eq. (13), with the same conditions than the ones used in the last MMLM case shown ($\mathrm{Re}_\lambda = 407$ and $k_{\max}\eta \approx 1$). The results for longitudinal velocity structure functions in this field are presented in Fig. 4. The two thin dashed lines in each plot show power laws of r according to Kolmogorov scaling exponents $\zeta_p = p/3$, and the scalings using the exponents generally reported in turbulent flows [21,34–37] are also shown (for orders $p=2$ and $p=4$ the Kolmogorov values are not shown). It is possible to see that the MTLM field presents a much better agreement with the known intermittent behavior in the inertial range than the previous cases obtained in Sec. III. There is a clear and systematic departure from the Kolmogorov scaling, and the slopes of the structure functions are remarkably close to the values associated with real turbulence. Specifically, the reference exponents used as comparison in Fig. 4 are an average of the experimental measurements of Ref. [34] for $\mathrm{Re}_\lambda = 515, 536, 852$. The average of the exponents obtained in direct numerical simulation (DNS) by Gotoh *et al.* [37] at $\mathrm{Re}_\lambda = 381, 460$ differ from the values used in the plots in a range of 0.4% to 1.7% for $p \leqslant 10$ (the exponent for $p=12$ is not available in this second reference). Applying the MTLM synthesizing method it is possible now to observe also inertial-range intermittency in a smaller case with 512^3 points. Conditions for this case are $\mathrm{Re}_\lambda = 253$ and $k_{\max}\eta \approx 1$, and the corresponding longitudinal structure functions for it

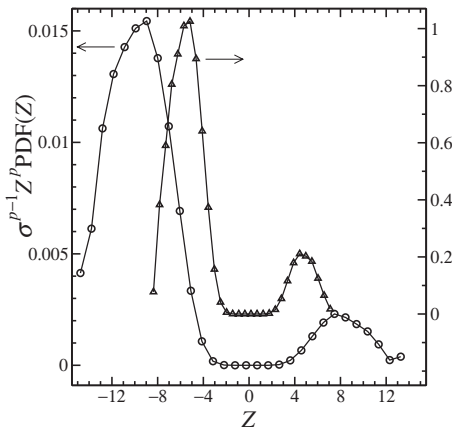

FIG. 5. Premultiplied PDFs (with $p=12$) for longitudinal velocity increments normalized by their standard deviations, $Z=\delta_\parallel u(r)/\sigma_r$, obtained with the 1024^3 MTLM field. ○ symbols and left vertical axis: $\log_{10}(r/\ell_M)=0.9$. △ symbols and right vertical axis: $\log_{10}(r/\ell_M)=1.6$

are also plotted in Fig. 4 (thick dashed lines).

For the functions of order $p=8$, 10, and 12, the good agreement covers a decade of scales. At small scales, the functions depart from the power-law trend at $\log_{10}(r/\ell_M)\approx 0.7$. This length is associated approximately with a wave number of $k\approx 2\pi/r=204$ (which corresponds to $k\eta=0.406$), being consistent with the wave number at which the drop off of the energy spectrum takes place at the high-wave-number end of the inertial range. A linear regression fitted (for the 1024^3 case) to the structure functions in the range $0.7\leqslant\log_{10}(r/\ell_M)\leqslant 2$ gives for the orders $p=8$, 10, and 12 the exponents $\zeta_8=2.235$, $\zeta_{10}=2.504$, and $\zeta_{12}=2.703$, respectively.

In order to check for appropriate convergence of statistics, we compute the PDFs for the longitudinal velocity increments $\delta_\parallel u(r)$ at different separation scales r for the highest order analyzed ($p=12$). Figure 5 shows the results for $\log_{10}(r/\ell_M)=0.9$, near the high-wave-number end of the inertial range and for $\log_{10}(r/\ell_M)=1.6$ well into the inertial range. Results for other r in the range $0.7\leqslant\log_{10}(r/\ell_M)\leqslant 2$ present similar behavior. Here Z is $\delta_\parallel u(r)$ normalized by its standard deviation σ_r and the curves show $\sigma_r^{p-1}Z^p\mathrm{PDF}(Z)$,

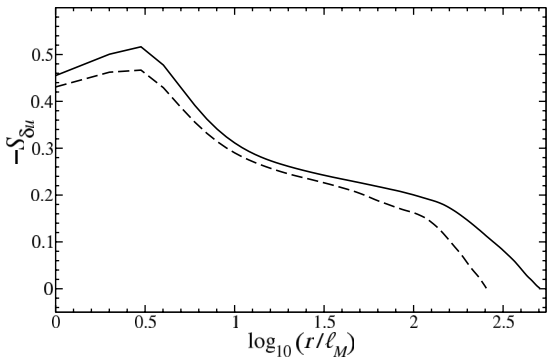

FIG. 6. Skewness of longitudinal structure functions as function of separation r between points. Solid line: 1024^3 field. Dashed line: 512^3 field.

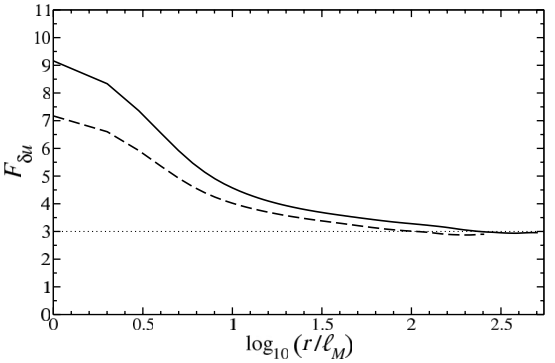

FIG. 7. Flatness of longitudinal structure functions as function of separation r between points. Solid line: 1024^3 field. Dashed line: 512^3 field.

which is equivalent to $[\delta_\parallel u]^p f(\delta_\parallel u)$, where f is the PDF for $\delta_\parallel u(r)$. These functions, when integrated, will give the pth-order moments, and we can see that the weighted PDFs are sufficiently smooth, particularly over the ranges that dominate the values of the integrals. For the case $\log_{10}(r/\ell_M)=0.9$, at the left end it can be seen that the weighted PDF is not entirely closed and thus the moment may be overestimated by a few percent. But the effect of this on the power-law behavior is negligible. Thus, we consider the statistics reasonably well converged for the orders of the structure functions obtained.

Figures 6 and 7 depict the skewness S and flatness F of the $\langle\delta u_\parallel\rangle$ functions at different separations for both fields. The general qualitative trend agrees well with the real turbulence behavior. The flatness and (negative) skewness grow slowly in the inertial range, and on approaching the dissipative range they undergo a very fast increment [38,39]. For $\log(r/\ell_M)=0$ the value of $\delta u_\parallel$ can be regarded as proportional to the derivative $\partial u_\alpha/\partial x_\alpha$ ($\alpha=1,2,3$; no summation). For both cases, the values of the flatness at that smallest numerically possible separation match correctly the experimental values in turbulent flows collected from various sources by [22]: $F\approx 8-9$ at $\mathrm{Re}_\lambda\approx 400$ and $F\approx 7-8$ at $\mathrm{Re}_\lambda\approx 250$.

In Fig. 8 we show the third-order structure function for the 1024^3 case. One can see that the MTLM field displays

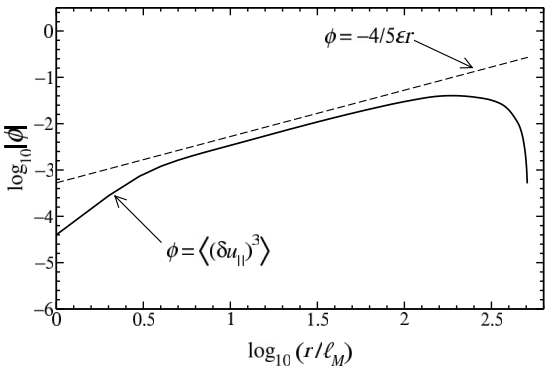

FIG. 8. Third-order longitudinal velocity structure functions for the 1024^3 MTLM field. For the dashed line ε is the prescribed dissipation in the energy spectrum.

the correct trend of $\langle[\delta u_{\parallel}(r)]^3\rangle \propto r$ in the inertial range, which holds true even for an intermittent field. The straight line in the plot corresponds to the right-hand side term in Eq. (3), where ε is the constant value of dissipation that enters into the prescribed energy spectrum. The only difference between the synthetic and a true turbulent field is an undershoot in the proportionality constant; i.e., for the synthetic field, we obtain $\langle[\delta u_{\parallel}(r)]^3\rangle \approx -0.55\epsilon r$. It is useful to note that the physically realistic coefficient $-4/5$ arises from integration of the Kármán-Howarth equation, which itself comes from the dynamical Navier-Stokes equations. Since the MTLM procedure does not correspond to true Navier-Stokes dynamics, such quantitative differences are perhaps not surprising.

V. VORTICITY AND STRAIN-RATE FIELDS

Having established that the multiscale Lagrangian map with a turnover time scale is able to generate non-Gaussian velocity fields endowed additionally with realistic inertial-range anomalous scaling, it is of interest to study again some aspects of the geometrical structure of the velocity field, such as the spatial organization of the vorticity and strain rate. Figure 9(a) shows contours of vorticity magnitude ω in a slice of the 1024^3 MTLM field. The central 128^2 subregion of this slice is shown magnified in the Fig. 9(b) view. The values of ω have been normalized by the maximum vorticity in the complete field. For scale reference, lengths corresponding to L and to 50η are indicated in the plots. Note that the formats of these figures resemble somewhat those used in Ref. [40] for DNS results, but show bidimensional cuts instead of three-dimensional isosurfaces. Figures 9(c) and 9(d) present the vorticity magnitude at the same positions for the initial Gaussian field.

The general structure of the spatial distribution of vorticity is similar to the one observed in [14] for a smaller field generated with the synthesizing procedure of Sec. III, which does not produce inertial-range anomalous scaling. The strong vorticity appears concentrated in thin elongated regions embedded in a background of weak vorticity which occupies most of the volume. By contrast, the initial vorticity had a structureless fine-grained pattern uniformly distributed. For the MTLM case, some of the region of concentrated vorticity have lengths of more than 300η, while their thickness is comparable to the smallest resolved scale ℓ_M ($\approx 3\eta$). Although at first sight the set of thin objects in these bidimensional views could resemble the tangle of vortex filaments characteristic of turbulent fields, they are instead cuts through more or less 2D surfaces of isovorticity, as detailed scanning of the whole field and three-dimensional plots of isovorticity have revealed. Like in the results obtained with the unmodified MMLM method, the concentration of vorticity takes place in the form of vortex sheets and no clear evidence of vortex tubes or vortex filaments are seen. The strain rate (not shown) is highly correlated with the vorticity, and therefore cuts through the local energy dissipation field are qualitatively very similar in appearance to Fig. 9.

Figure 10 shows conditional averages of enstrophy production,

$$\sigma \equiv \omega_i \omega_j S_{ij} \tag{19}$$

[where $S_{ij}=\frac{1}{2}(\partial_i u_j + \partial_j u_i)$ is the strain-rate tensor], while Fig. 11 shows conditional averages for the generation of strain by self-amplification,

$$\Pi \equiv -2S_{ij}S_{ik}S_{kj}, \tag{20}$$

and for the combined term,

$$\Sigma \equiv -2S_{ij}S_{ik}S_{kj} - \frac{1}{2}\omega_i \omega_j S_{ij}, \tag{21}$$

acting as the inviscid and pressureless part of the rate of generation of strain in the governing equation for $|\mathbf{S}| \equiv S_{ij}S_{ij}$ [41]. The quantities are conditioned on regions of different intensities of strain and vorticity with respect to the mean field values.

These statistics are presented in the same form as it is done in Ref. [14] for MMLM synthetic turbulence and in Ref. [41] for real turbulence. The results are essentially the same as those obtained for the MMLM field without anomalous scaling: the behavior is quite consistent with the one observed in real turbulence [41] for the strain-dominated regions, but the same quantities conditioned on vorticity-dominated regions tend to follow the trends of the strain-dominated region, in a damped way, instead of showing a very weak dependence on vorticity intensity as occurs for the real turbulent flow. In real turbulence the statistics conditioned over regions with the strongest vorticity are dominated by vortex tubes or filaments, which are relatively passive in comparison with the regions of strongest strain, being mostly distorted by the part of the strain upon which they do not react, and not by self-amplification. As a consequence, these regions do not present a particularly high local enstrophy generation (see [42,43]).

The PDFs of vorticity and strain-rate magnitudes for the 1024^3 MTLM field are shown in Figs. 12 and 13. The same figures also show the corresponding PDFs for MMLM and Gaussian fields of the same size. The MTLM vorticity presents the same behavior as observed in turbulence DNS (e.g., compare with Fig. 15 of Cao *et al.* [44]). The PDFs reflect the high intermittency of the vorticity and dissipation in the MTLM field. For the MMLM case, on the other hand, the intermittency of these small-scale properties, although still higher than Gaussian levels, are considerably lower. The accumulation of enough distortion at the end of the sequence of scales is thus crucial in determining proper levels of intermittency in the synthetic fields. Interestingly, the crossing of the synthetic fields PDFs over the Gaussian ones occurs around $\omega/\omega_{\mathrm{rms}}=1.8$ and $|\mathbf{S}|/|\mathbf{S}|_{\mathrm{rms}}=1.8$, which are the same values found in DNS in Ref. [44]. From these PDFs we can see also that the distribution of vorticity and strain (and thus dissipation) are approximately the same in the synthetic field. This is consistent with the observation that the zones of high vorticity in these fields tend to coincide with the zones of intense strain-rate.

These observations support the previous statement about the absence of vortex-tube structures in the synthetic field. Notwithstanding the enhanced distortion introduced at each scale level in the MTLM case compared with the simpler

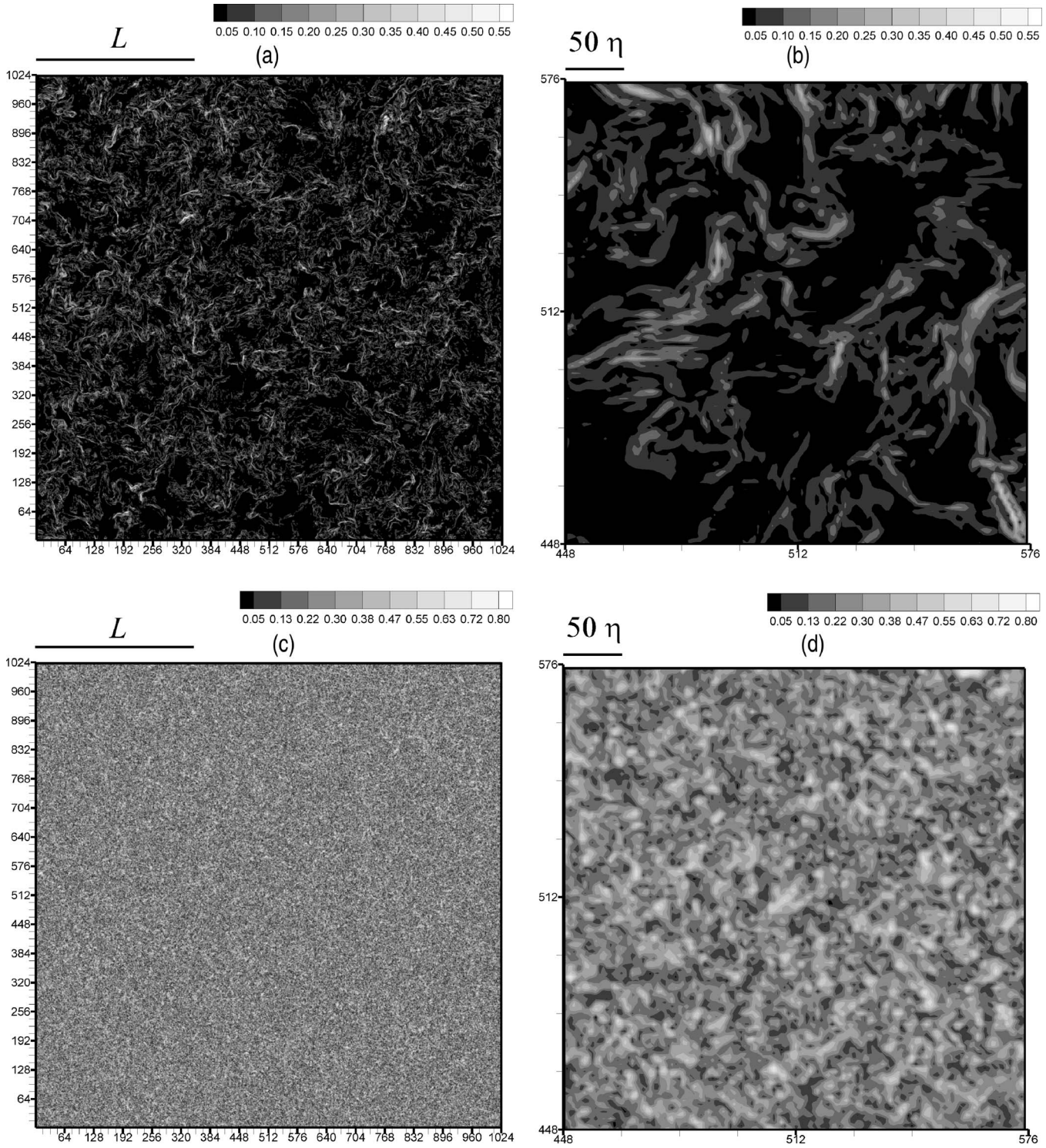

FIG. 9. Contours of isovorticity. (a) 1024^2 slice in the MTLM field. (b) Zoom-in view for the 128^2 central subregion in (a). (c) 1024^2 slice in the initial Gaussian field. (d) Zoom-in view for the 128^2 central subregion in (c).

MMLM case, spatial formations akin to vortex-tube are not produced by the Lagrangian mapping. Since several studies (e.g., [45,46]) have concluded that such structures are formed by instabilities of existing vortex sheets (at least in homogeneous turbulence), the vorticity distribution produced by the map resembles an early stage of their development. It seems that the mechanism involved in their final formation is too complex to be captured, even in a rudimentary way, by the very simple kinematics and minimal dynamics encompassed by the mapping and projection process. On the other hand, the production of vortex sheets appears as natural, given the tendency of the mapping to generate converging streams, which can be related with two extensional and one contractive principal strain. Recall that in the advancement from one

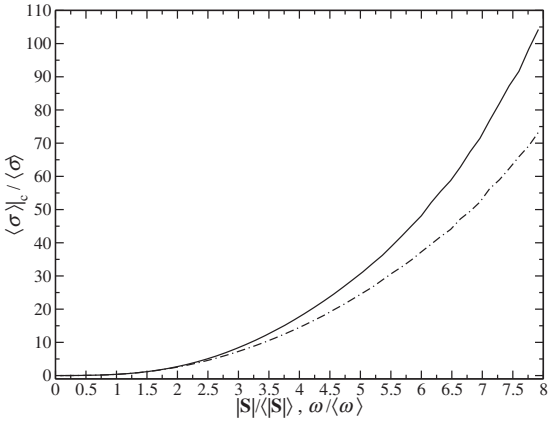

FIG. 10. 1024^3 MTLM field: conditional averages of enstrophy generation σ. Solid line: conditioned on $|\mathbf{S}|/\langle|\mathbf{S}|\rangle$. Dot-dashed line: conditioned on $\omega/\langle\omega\rangle$.

level to the next one in the sequence of scales, a new band of higher wave numbers (associated with still Gaussian modes) is added to the range of wave numbers over which the mapping has already acted. Thus, at a given level, the low-pass-filtered velocity field generated in the previous level can be regarded as a large-scale distortion with respect to the vorticity field of the new additional band. The prevalence in the larger-scale field of the strain state mentioned above will flatten the additional incoherent vorticity into more localized sheets. As discussed in [47], the direct production of a vortex tube by such kind of strain in a multiscale vortical flow requires very special conditions (related generally with the small-scale vorticity located symmetrically with respect to the large-scale strain), which are unlikely to occur in a random field.

VI. MULTIFRACTAL ANALYSIS OF THE DISSIPATION

The concentrated spatial distribution of vorticity modulus as seen in Fig. 9 is an indication also of strong nonuniformity

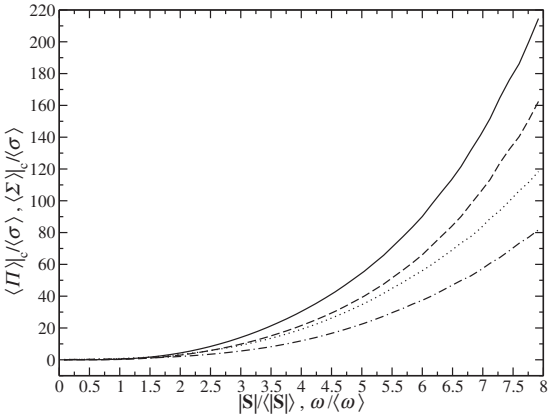

FIG. 11. 1024^3 MTLM field: conditional averages of strain production terms Π and Σ, normalized by the mean enstrophy generation $\langle\sigma\rangle$. Solid line: Π conditioned on $|\mathbf{S}|/\langle|\mathbf{S}|\rangle$. Dashed line: Σ conditioned on $|\mathbf{S}|/\langle|\mathbf{S}|\rangle$. Dotted line: Π conditioned on $\omega/\langle\omega\rangle$. Dot-dashed line: Σ conditioned on $\omega/\langle\omega\rangle$.

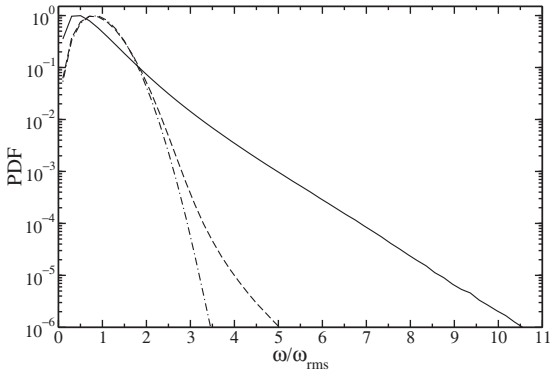

FIG. 12. PDF for vorticity magnitude ω for 1024^3 fields. Solid line: MTLM field. Dashed line: MMLM field. Dot-dashed line: Gaussian field.

of the energy dissipation [the local dissipation at a given position being equal to $\nu(\omega_i\omega_i+2\partial_j u_i \partial_i u_j)$]. To avoid confusion with the mean energy dissipation ε over the whole field, the local dissipation field at position $\mathbf{x}$ will be denoted as $\tilde{\varepsilon}$ and is determined by the strain-rate tensor as

$$\tilde{\varepsilon}(\mathbf{x}) = 2\nu \mathbf{S}(\mathbf{x}):\mathbf{S}(\mathbf{x}). \tag{22}$$

In this section $\tilde{\varepsilon}$ will be referred to simply as the dissipation. The conventional thinking of the turbulent energy transfer among scales as a cascade process from larger to smaller eddies until reaching dissipative scales has led to the idea that the characteristics of this process can be manifested in the final product at the end of the cascade—namely, the energy dissipation [48]. A cascade (or a multiplicative process) can usually be described using the multifractal formalism, which is especially well suited for the description of strongly intermittent measures [21,49,50]. The specific measure density considered in turbulence is $\tilde{\varepsilon}(\mathbf{x})$. The cumulative dissipation E_r in a region Ω of size r centered at $\mathbf{x}$ is

$$E_r(\mathbf{x}) = \int_{\mathbf{x}' \in \Omega(\mathbf{x};r)} \tilde{\varepsilon}(\mathbf{x}') d^3\mathbf{x}', \tag{23}$$

and the total dissipation in the whole domain of size H will be denoted as E_t. For definiteness, the regions Ω will be

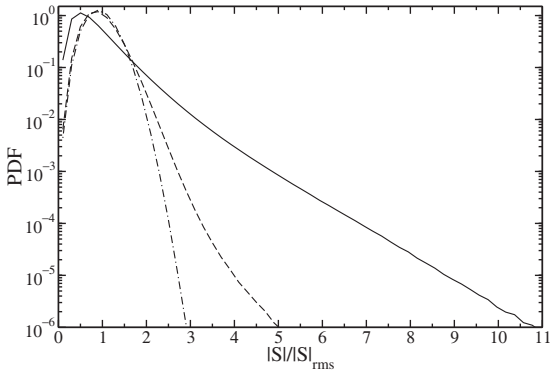

FIG. 13. PDF for strain-rate magnitude $|\mathbf{S}|$ for 1024^3 fields. Solid line: MTLM field. Dashed line: MMLM field. Dot-dashed line: Gaussian field.

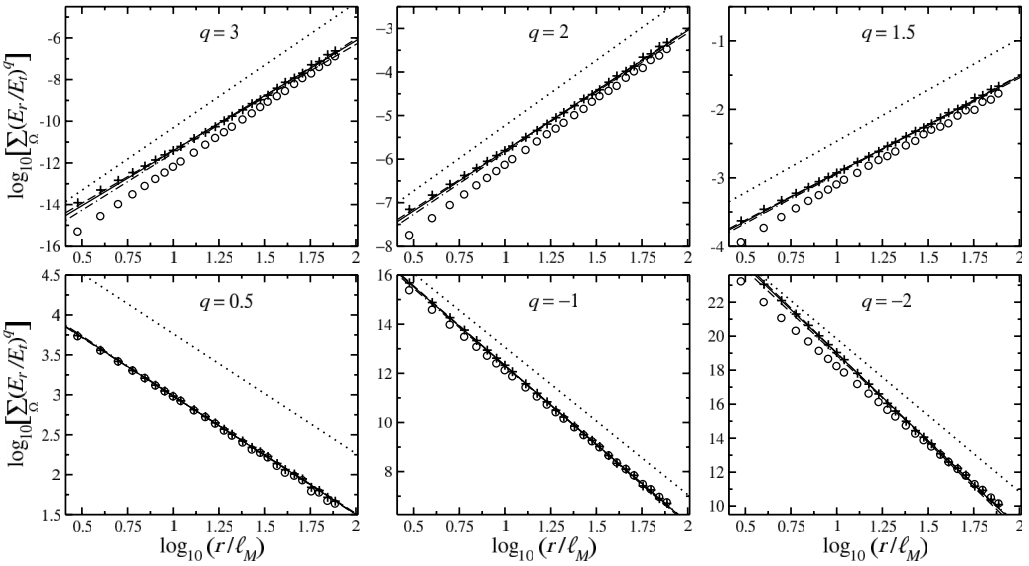

FIG. 14. Moments of the normalized cumulative dissipation for the indicated order q, as function of the size r of the Ω box. +: results for a 1024^3 MTLM field. ○: results for a 1024^3 MMLM field. Dotted lines: K41 scaling. Solid lines: fitting over range $A=0.81<\log_{10}(r/\ell_M)<1.81$ $(20<r/\eta<200)$. Dashed lines: fitting over range $B=0.81<\log_{10}(r/\ell_M)<1.51$ $(20<r/\eta<100)$. Dot dashed line: fitting over range $C=1.11<\log_{10}(r/\ell_M)<1.81$ $(40<r/\eta<200)$.

taken as boxes of side length r centered at the position $\mathbf{x}$.

The characterization of a multifractal can be given in terms of Renyi dimensions D_q or by the singularity spectrum [24]. After covering the volume with equal boxes of size r, a local scaling relation is written as $E_r/E_t \sim (r/H)^\alpha$ and the Hölder exponent α quantifies the strength of the singularity at $\mathbf{x}$ as $r\to 0$. For a multifractal, E_r scales with many different exponents α on corresponding different sets of fractal dimension $f(\alpha)$. The function $f(\alpha)$ is the singularity spectrum. Note that the scaling relation for E_r/E_t implies that the dissipation averaged over the boxes of size r scales as $\varepsilon_r/\varepsilon \sim (r/H)^{\alpha-3}$, and thus singular behavior as $r\to 0$ occurs for $\alpha<3$.

A scaling relation can be written also for the sum of E_r^q over all disjoint Ω boxes of size r,

$$\sum_\Omega \left(\frac{E_r}{E_t}\right)^q \sim \left(\frac{r}{H}\right)^{\tau(q)}, \tag{24}$$

and the singularity spectrum is given as a Legendre transform of the moment exponents $\tau(q)$,

$$f(\alpha(q)) = q\alpha(q) - \tau(q), \tag{25a}$$

$$\alpha(q) = \frac{d\tau}{dq}. \tag{25b}$$

Computation of the sums $\Sigma_\Omega (E_r/E_t)^q$ are carried out for 43 values of q in the interval $q\in[-2,3.25]$, over all possible disjoint boxes of size $9.3\leqslant r/\eta\leqslant 238$ in the 1024^3 field. This interval of scales allows to encompass a substantial part of the dissipative and inertial ranges. At larger r the number of boxes becomes too small for statistical sampling. Results of $\Sigma_\Omega (E_r/E_t)^q$ for representative values of q are shown in Fig. 14. A power-law behavior consistent with Eq. (24) is well satisfied in general terms for all the q values considered, becoming a little more ambiguous, but still reasonable, for the higher exponents. Least-squares regression was used to obtain the moment exponents $\tau(q)$ from the data. For this purpose the fittings should be restricted to a range of r values where the viscous damping introduced by the imposed spectrum is not expected to affect the results. This lower limit is known to be around $r/\eta>20$ in real turbulence. On the other hand, to remove effects from the large-scale range, scales corresponding to $r>0.2L$ (where L is the integral length scale) are also excluded. This determines a range of $0.81<\log_{10}(r/\ell_M)<1.81$, which is referred to as "range A" in the following (since $\ell_M=3.09\eta$, the range corresponds to $20<r/\eta<200$).

In order to get a sense of variability of the results because of the uncertainty in the proper scaling range, we take also two additional ranges that modify by a factor of 2 the lower or upper bound of r/η in range A: range B for $0.81<\log_{10}(r/\ell_M)<1.51$ and range C for $1.11<\log_{10}(r/\ell_M)<1.81$. The cases shown in Fig. 14 display the fittings over these three ranges of scales.

Figure 15 presents the exponents $\tau(q)$ obtained using range A for the fitting (using +). Note that for a nonintermittent space-filling dissipation, as would be implied by the K41 theory, the dimensions D_q would be equal to 3 for all q and therefore $\tau(q)$ would be given by the linear function $\tau(q)=3(q-1)$ (shown as the dotted line). For comparison, the figure also shows the exponents obtained from a field synthesized with the MMLM procedure of Sec. III (open circles) for the same conditions. Interestingly, and consistent with the results of structure function scaling, the MMLM method produces essentially a K41 scaling.

The singularity spectrum $f(\alpha)$ is obtained from the exponents $\tau(q)$ applying Eqs. (25), and it is shown in Fig. 16 for the three scaling ranges aforementioned, along with data taken from Ref. [24], coming from experimental observations in laboratory and atmospheric flows. The spectrum for

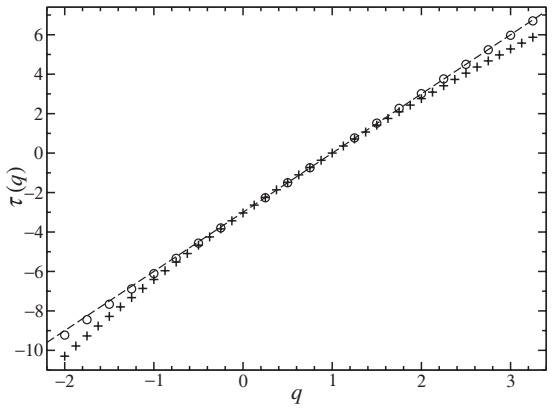

FIG. 15. Moment exponents as function of q obtained from the scaling relation (24). +: for a 1024^3 MTLM field ○, for a 1024^3 MMLM field; dashed line, K41 scaling.

the synthetic field resembles reasonably well the observed behavior in real turbulence, and there is good quantitative agreement in the core region $2.5<\alpha<3.5$. For the right tail of the spectrum, the synthetic $f(\alpha)$ does not decay as fast as in the experimental data, while the agreement is better on the left tail. Recall that the higher α exponents correspond to the moments of higher negative orders q, while the lower α values are associated with the higher positive q's. Thus, besides the obvious fact that the extremes of the spectrum are likely to be more affected by the uncertainty in the proper scaling range, we have to consider also that the negative order moments emphasize the smallest (near zero) values of the dissipation in the field. These zones of low dissipation arise mainly in the regions where the Lagrangian mapping produces a relative depletion of fluid particles, so that the interpolation gives a reduced local velocity gradient (as complementary to the regions where convergence of fluid particles takes place originating high velocity gradients and dissipation). Because of the characteristics of the construction of the

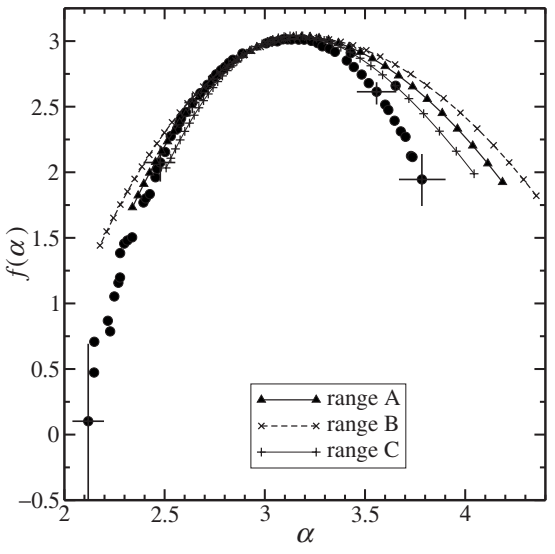

FIG. 16. Singularity spectrum $f(\alpha)$ obtained by Legendre transform of results in Fig. 15. Solid circles correspond to experimental data from Ref. [24].

velocity field, the structure of those regions of smoothed velocity distributions and depressed turbulence intensity are set mostly during the first stages of the synthesizing procedure (i.e., by the deformations introduced at the larger scales in the sequence), while the zones of high dissipation, emphasized by $q>0$, are the result of the accumulation of distortion over distortion of the local velocity field. In this sense the procedure acts more effectively in the build up of the most singular regions than in the development of the most regular ones. This can explain why the agreement on the left side of the singularity spectrum is better than on its right side.

The good agreement in the core of the spectrum suggests that some important characteristic features of the multifractal nature of the turbulent dissipation are reproduced well by the MTLM approach. For the discussion below we take range A as the base line for comparison, and the results for ranges B and C are indicated in parentheses in that order. The value of $f(\alpha)_{\max}$ occurs for $q=3.18$ (3.21, 3.16) in the synthesized case, which falls close to the value $q\approx 3.13$ found in the turbulent spectrum. $f(\alpha)_{\max}$ is equal to $D_0=3$, the dimension of the embedding space. More important is the dimension D_1 (the information dimension) which is the dimension of the set that contains asymptotically most of the dissipation. D_1 is equal to $\alpha(q=1)$, and this is also the α value that satisfies $f(\alpha)=\alpha$ [since $\tau(q=1)=0$ from relation (24)]. The value of D_1 derived in this way from the spectrum of the synthetic field is $D_1=2.89$ (2.85,2.93), which agrees well with the value $D_1\approx 2.87$ found in real turbulence [24]. It is also possible to compute the intermittency exponent μ [defined traditionally such that $\langle \varepsilon_r^2\rangle/\varepsilon^2 \sim (L/r)^{\mu}$, for $\eta<r\ll L$]. For low moment orders the lognormal approximation is valid, which is equivalent to a quadratic shape for $\tau(q)$, and one can find that [24]

$$\mu = -\left.\frac{d^2\tau(q)}{dq^2}\right|_{q=0}. \tag{26}$$

The result obtained from the curves in Fig. 15 (numerically obtained with tenth-order interpolation) is $\mu=0.33$ (0.41, 0.25). This is somewhat larger but still within the range of often cited experimental estimates for μ, which are in a range $\mu=0.25\pm 0.05$ (Ref. [51]) in real turbulence. Thus we find that MTLM synthetic fields display multifractality in the implied dissipation field, with intermittency levels that are slightly stronger, but still comparable to those of real turbulence. Conversely, with a non-Kolmogorovian (CFL) time scale applied to the distortions at each scale, the dissipation field remains essentially K41 like, without intermittent scaling. Hence, it appears that in order for intermittency to build up, it is imperative that the small scales be allowed to evolve at least during a time equal to their "turnover" time scale.

VII. INDUCED PRESSURE FIELD

In this section we analyze briefly the pressure field induced by the mapping procedure. Although no pressure forces act during the inertial movement of the particles to their new positions, the projection operation applied in Fourier space to restore the divergence-free condition has an

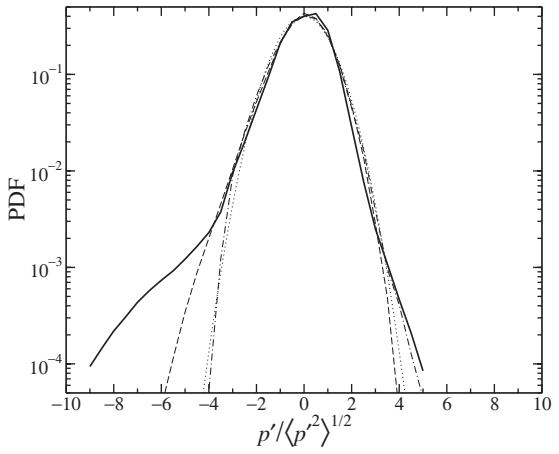

FIG. 17. PDF of normalized pressure fluctuations, obtained from (solid line) 1024^3 synthetic MTLM field, (dot-dashed line) 1024^3 synthetic MMLM field, and (dashed line) 1024^3 Gaussian field. The dotted line is a normalized Gaussian distribution.

effect similar to the pressure in a real incompressible flow, which constrains the velocity field to be solenoidal. Once the synthesizing procedure has finished, one is left with a solenoidal velocity field. If we regard this field as it were the velocity of an incompressible fluid flow, then it is possible to obtain an inherent pressure distribution by solving the Poisson equation

$$\nabla^2 p = -\partial_j u_i \partial_i u_j = \frac{1}{2}\boldsymbol{\omega}\cdot\boldsymbol{\omega} - \mathbf{S}:\mathbf{S}, \tag{27}$$

where p is the pressure divided by the density (since the density is constant and its value is immaterial here, we will call p the pressure). We stress that Eq. (27) is not derived from any dynamical relation in the synthesizing procedure, but we are using the Poisson equation to assess the statistical features of an equivalent pressure implicit in the synthetic velocity field.

Since the pressure is the solution of a Poisson equation, a negative skewness for the pressure fluctuation will arise if the right-hand side (RHS) of the equation is positively skewed. Negative fluctuations can be expected then predominantly in regions where the RHS is positive and, in view of Eq. (27), this means that negative pressure fluctuations are associated mainly with regions where enstrophy is dominant over the strain rate, which in turbulent flows are identified chiefly as vortex tubes and filament structures. Indeed, the numerical results in [44] showed that in very-low-pressure regions, the pressure structure was mostly composed of filaments or tubelike structures. This link between low-pressure and vortex filaments has been observed also experimentally [52].

The pressure is calculated for the 1024^3 MTLM field obtained in Sec. IV solving for $\hat{p}$ in Fourier space. Figure 17 shows the PDF for the pressure fluctuations $p'=p-\langle p\rangle$ normalized by its standard deviation. The figure also shows the corresponding distributions for pressure fluctuations obtained from the 1024^3 MMLM field and from a 1024^3 Gaussian field. The distribution for the MTLM field is negatively skewed and displays a prominent tail at the negative fluctuations side, while at the positive side it is closer to a Gaussian profile. This form for the PDF is in agreement with observations for Navier-Stokes turbulence in several DNS studies [44,53–58], and it has also been obtained in experiments [59]. In addition, for the synthetic MTLM pressure field shown here we obtain a ratio $p'_{\mathrm{rms}}/u^2_{\mathrm{rms}}=0.73$, not inconsistent with prior DNS results. The skewness coefficient of pressure, S_p, is considered next. Reported values in [56] at different Reynolds numbers (up to $\mathrm{Re}_\lambda=235$) show that it remained roughly constant in a range of $-1.07<S_p<-0.88$. Similar behavior and values were found also in [44,55]. For the MTLM synthetic field, the value obtained here is $S_p=-0.96$, in good agreement with observed values.

The distribution for the Gaussian field is already negatively skewed ($S_p=-0.38$). This is a well-known fact [44,55,57,60] that has been associated with the specific form of the Poisson equation solution and the nonlinear combination of the Gaussian gradients on its source term. On the other hand, the negative skewness for the MMLM case is weaker ($S_p=-0.16$). We do not have a clear explanation for this sub-Gaussian behavior of the pressure field of the MMLM case, but point out that it is reminiscent of the results obtained in low-Reynolds-number DNS [57]. They observed that at low Reynolds numbers, the pressure field also had a negative tail that fell under that of the pressure arising from a Gaussian field. Perhaps the lower intermittency levels of MMLM correspond to what occurs in real turbulence at low Reynolds numbers.

The key distinction between the MTLM and MMLM cases is the increased intermittency for the MTLM case at the smallest scales (as seen in the PDFs of Figs. 12 and 13). Hence, even though for the MTLM fields the intense enstrophy and the intense strain still tend to coincide, the high intermittency levels produce an increment in the magnitude of local enstrophy and strain differences and the frequency of large excursions, so that the pressure source term becomes more effective. The main difference with respect to real turbulence is that these regions of dominant enstrophy and low pressure occur on sheetlike structures instead of filaments. It is reasonable to assume that these sheets are precursors from which the filaments will finally evolve and differentiate upon the action of the true dynamics. This premise is consistent with the observation of [58] in DNS of decaying isotropic turbulence, where the low-pressure regions were found to be sheetlike at early evolution times and organized as slender filaments later on for fully developed turbulence.

Another important characterization of the pressure field is the (three-dimensional) spectrum of pressure fluctuations, $E_p(k)$, defined such that

$$\langle (p-\langle p\rangle)^2\rangle = \int_0^\infty E_p(k)dk. \tag{28}$$

If the Kolmogorov hypotheses are applied to the local statistics of the pressure, the form

$$E_p(k) = B\varepsilon^{4/3}k^{-7/3} \tag{29}$$

is found in the inertial range [20], where B is a constant coefficient. The experimental measurements of [59] support

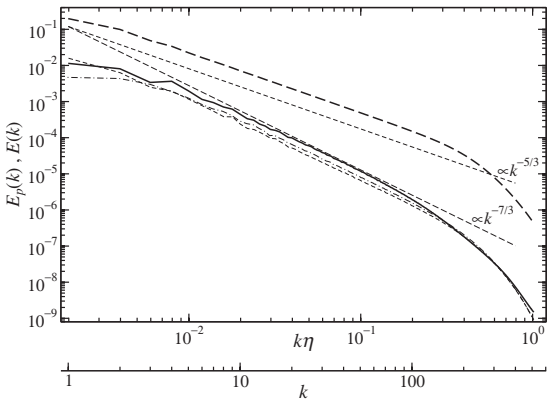

FIG. 18. Pressure spectrum $E_p(k)$. Solid line: for the 1024^3 MTLM synthetic field. Dashed line: for the 1024^3 MMLM synthetic field. Dot-dashed line: for a 1024^3 Gaussian field. The thick dashed line is the imposed energy spectrum $E(k)$.

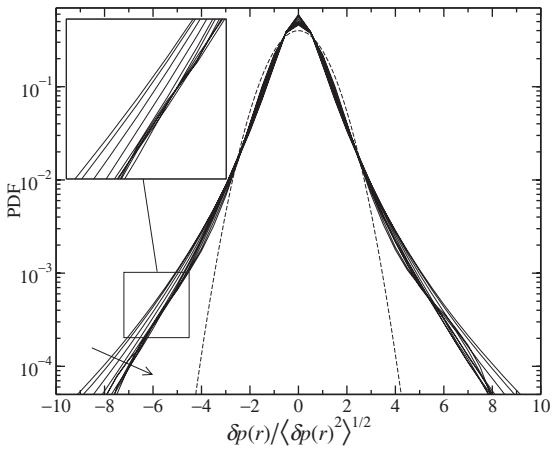

FIG. 19. PDF of pressure increments for separations $r/\ell_M = 1,2,4,8,16,32,48,64,92,128$ in the direction of the arrow. Dashed line is a normalized Gaussian distribution.

the $-7/3$ scaling of the pressure spectrum for $\mathrm{Re}_\lambda > 600$, and similarly DNS studies with 2048^3 resolution [40,61] have given results that approach a $-7/3$ power-law.

The pressure spectrum obtained for the synthetic MTLM field is shown in Fig. 18. It displays indeed a trend that departs from a $-5/3$ scaling and converges to a $-7/3$ law in the inertial range. An average $-5/3$ scaling could only be fitted over a small range of low wave numbers corresponding approximately to the ten lowest wave-number shells, but for higher wave numbers the slope clearly tends to $-7/3$. The interval over which the $-7/3$ law approximately holds is, however, narrow in comparison with the range of (imposed) $-5/3$ scaling for the kinetic energy spectrum, also shown in the graph. All of these characteristics resemble the behavior observed in DNS of turbulence. For simulations with Reynolds numbers lower than the imposed $\mathrm{Re}_\lambda = 407$ of the synthesized case, a very narrow range with $E_p(k) \sim k^{-7/3}$ has been observed in DNS, along with a wider interval where $E_p(k) \sim k^{-5/3}$ (e.g., in [56]), suggesting two scaling ranges. The computation of [61] at $\mathrm{Re}_\lambda = 732$ has clarified that $E_p(k)$ tends to behave as $E_p(k) \sim k^{-7/3}$ in DNS. But even at that high resolution, the approach is slow and over a rather limited interval, similar to what is seen in Fig. 18, but for a wider range of wave numbers. In the experiments of [59] the range of $-7/3$ scaling for the pressure spectrum is also almost one decade shorter (at the low-wave-number side) than the range of $-5/3$ scaling for the energy spectrum, at $\mathrm{Re}_\lambda = 1170$. Hence, the characteristics of the spectrum of synthetic pressure fluctuations, including the difficulty to clearly resolve the $-7/3$ scaling range at the given Reynolds number, are not different of what is seen in real turbulent flows.

The spectra for a Gaussian field and for a MMLM field are also shown in Fig. 18. As expected, for the Gaussian case the $-7/3$ scaling is achieved more easily and over an extended range. The pressure spectrum for the MMLM case follows a similar trend than the MTLM one, but its drop-off at the high-wave-number end of the velocity inertial range occurs around the same wave number than does the energy spectrum, as in the Gaussian case. In contrast, the drop-off for the MTLM spectrum takes place at a significantly smaller wave number, presenting a more early departure from the $-7/3$ scaling in spite that the kinetic energy is enforced to follow a $-5/3$ law. This shows again the breakdown of Kolmogorov scaling in the MTLM field as intermittency emerges.

Figure 19 presents the PDF of pressure increments $\delta p(r) = p(\mathbf{x}+\mathbf{r}) - p(\mathbf{x})$. By contrast to the typical PDFs of velocity increments, where the strong deviation from a Gaussian distribution decreases progressively as the separation r grows, the PDFs for pressure increments display conspicuously stretched-exponential behavior for almost the entire range of $\delta p(r)$. As r continues to grow in the inertial range, the distributions for the larger separations start accumulating and the statistics remain markedly non-Gaussian, as the zoom-in view in the plot shows. The entire behavior is similar to the observations in DNS of real turbulence [44,56] where the persistence of non-Gaussianity at large separations is explained by the long-range action of the pressure. In the current synthetic case this nonlocal effect comes evidently from the projection in wavenumber space, which can change the velocities in the whole domain.

The second-order pressure structure function will scale as $\langle [\delta p(r)]^2 \rangle \sim r^{4/3}$ when the pressure spectrum is given by Eq. (29). More generally, the Kolmogorov-type dimensional argument applied to the mth-order pressure structure function gives

$$\langle [p(\mathbf{x}+\mathbf{r}) - p(\mathbf{x})]^m \rangle \sim \varepsilon^{2m/3} r^{2m/3}, \tag{30}$$

for r in the inertial range. This relation will be affected also by intermittency. Some authors (see, e.g., Ref. [62]) have conjectured that if the hypothesis, on dimensional grounds, of similar scaling for pressure and velocity square is extended to increments of pressure and velocity, one could expect that the intermittency exponents of the velocity field can be applied also to the pressure scaling, so that Eq. (30) could be corrected as

$$\langle [p(\mathbf{x}+\mathbf{r}) - p(\mathbf{x})]^m \rangle \sim r^{\zeta_{2m}}, \tag{31}$$

where ζ_{2m} is the exponent for the $2m$th-order velocity structure function. This is a controversial point, and at present no

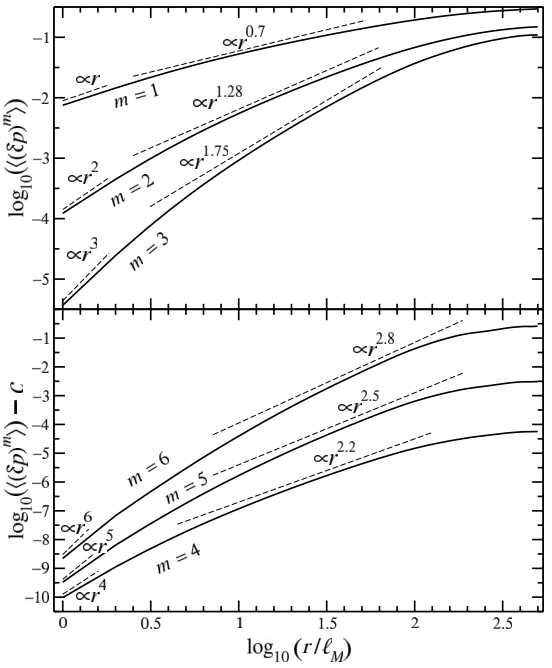

FIG. 20. Pressure structure functions of order m for the synthetic field. For clarity, in the lower graph the curves have been shifted vertically by $c=3.3$ for $m=4$ and by $c=1.7$ for $m=5$ ($c=0$ for $m=6$).

clear verification, numerical or experimental, of Eq. (31) is available. The argument of pressure scaling in the same way as the local kinetic energy was questioned by Nelkin [63]. Hill and Wilczak [64] derived an exact relation for $\langle[\delta p(r)]^2\rangle$ in terms of linear integrals of fourth-order velocity structure functions, which gives support to Eq. (31) for $n=2$. However, it has been shown [65,66] that there is a strong cancellation among the contributions to $\langle[\delta p(r)]^2\rangle$ from the velocity structure functions in the Hill-Wilczak relation, so that a considerably higher Reynolds number is required for inertial range scaling of the pressure than for inertial range scaling of the velocity. DNS has not produced a clear inertial range for pressure structure functions from which scaling information can be extracted (in addition, Ref. [65] shows that pressure scaling properties are highly sensitive to small differences between the scaling of longitudinal and transversal velocity structure functions).

Only in order to document the trend for the synthetic MTLM field in this respect, we show in Fig. 20 results for $\langle[\delta p(r)]^m\rangle$, with $m=1,2,\ldots,6$. Slopes corresponding to the exponents ζ_{2m} for turbulence (same values as those used in Sec. IV) are indicated for reference, although no clear inertial-range scaling can be discerned. For r approaching zero the functions tend to the expected behavior as r^m. From Fig. 18 one can estimate $k\eta \approx 10^{-1}$ as the high-wave-number end of the inertial range for pressure scaling, which is equivalent to $\log_{10}(r/\ell_M)\approx 1.4$. For the higher computed orders 4, 5, and 6 the slope of the functions seems to stay close to the ζ_{2m} values for a narrow range when $\log_{10}(r/h)>1.4$, while for the lowest orders the slope is somewhat smaller. In all the cases the slope for inertial range separations is clearly depressed with respect to the value $2m/3$ of the nonintermittent dimensional argument.

VIII. CONCLUSIONS

In this paper we have extended our study about the capabilities of the minimal multiscale Lagrangian map to reproduce statistical and geometrical features of hydrodynamic turbulence. In this approach, the multiplicity of characteristic spatial scales of turbulence is introduced by a hierarchy of velocity fields defined on sets of points distributed at different separations and the non-Gaussianity stems from the distortion of these fields by the action of a Lagrangian mapping. This mapping represents the simplest motion that fluid particles would follow if all interacting forces were momentarily suppressed. Nonlocal effects are reintroduced by the projection of the whole velocity field onto its divergence-free part. For this system, the characteristic spatial scales are naturally the separation between points at each set in the hierarchy. On the other hand, the degree of distortion introduced at each scale depends on the timelike parameter of the mapping. The buildup of non-Gaussian statistical moments for velocity gradients and increments originates in the emergence of zones where particle trajectories converge in a somewhat organized way, coming from points whose velocities were correlated at the beginning of the motion. Since the velocity fields on each set of points are initially smooth at that particular scale (after all wave numbers higher than the cutoff defined by that scale have been filtered out), velocities of neighboring points are correlated, and thus the appropriate displacements should be comparable to the separation between points. This CFL-like mapping time given by Eq. (7), which restricts the magnitude of particle displacements to be of the order of the separation between points, was used in the previous work [14]. That synthesizing procedure was shown to reproduce many important turbulent characteristic associated with statistical moments of orders 3 and 4, including key nonlinear energy transfer mechanisms related to velocity gradients, as well as geometric alignment trends.

In the present paper we have focused mainly on the intermittency and scaling properties of the synthetic velocity field in the inertial range, and we find that with a mapping parameter according to Eq. (7) no significant anomalous scaling of the velocity structure functions appears in the inertial range. Although that parameter is sufficient to generate the low-order moments, the deformation of the velocity field induced by the mapping becomes progressively weaker as the length scale is reduced. With the form given by Eq. (7) the time parameter is not related to the intrinsic dynamics of the turbulent cascade, but only to the "sweeping time scale." A modified procedure has been explored for which the mapping parameter is calculated in a way such that the accumulated distortion generated takes place, on average, during the "Lagrangian local eddy turnover time" particular for each scale. Results obtained with this second form are found to reproduce adequately the anomalous scaling phenomenon. In addition, the behavior of the velocity gradients skewness and flatness shows an improvement, compared with the results of the original MMLM approach, in the dissipative range. Further analysis of the vorticity and strain-rate fields confirms the previous observations [14] about the organization of the vorticity in vortex-sheet-like structures and the absence of vortex filaments. In regard to the spatial structure of energy

dissipation in the synthesized field, this is examined by means of the multifractal analysis for measures and its singularity spectrum is determined. The results are in reasonably good agreement with the known multifractal characteristics of dissipation in real turbulence. Consistent with the analysis of structure functions, the dissipation field generated using the MMLM approach yielded no multifractal scaling.

To further characterize the MTLM synthetic fields, some basic statistics have been analyzed for the pressure field implied by the velocity distribution. Comparison with turbulent data from different sources shows that fundamental properties such as probability distributions of pressure fluctuations, the spectrum of these fluctuations, and distributions of pressure increments behave in a similar way to their counterparts in real turbulent flows.

Two of the key components of turbulence are the self-distortion of the velocity field and the multiscale structure of the field. The first of these components is provided in our synthetic case by the Lagrangian map, while the second is explicitly introduced by the hierarchy of scales used. The construction of the velocity field is essentially kinematical, without any continuous dynamical effect to produce smaller scales from the larger ones, but in place of that the smaller scales (with Gaussian statistics) are directly introduced at each level in the sequence. Then they are allowed to be deformed by themselves and by the action of the larger scales that preceded them. The smaller scales are not directly an "offspring" of the larger ones, but instead they (with their initial Gaussian statistics) are added "by hand" onto the larger-scale velocity field. What stems directly from the large-scale field is the spatial distribution of locations where these additional fluctuations are more strongly distorted. The sequential cumulative deformation of these velocity fields in the synthesizing procedure plays the connective role between scales. In the synthetic case no dynamical energy transfer (energy cascade) takes place since the proper amount of energy at each scale is imposed by construction during the rescaling, via the energy spectrum. We have instead a kind of "cascade of spatial structure" by which spatial intermittency builds up from spatial inhomogeneities of the deformation that occurred at the large-scale velocity fields. To explore this point, additional tests were made where this "accumulation" of spatial intermittency was suppressed artificially. This was done by letting the velocity field at each scale be deformed as before and using the same mapping parameter as before, but using for each scale the initial Gaussian larger-scale velocities. In this way the effects of the distortion at the different scales are not passed down cumulatively, and they are combined only at the final step. In this case, the final velocity field remained basically Gaussian and no anomalous scaling was observed.

The results for the velocity structure functions and the dissipation indicate that in addition to the self-distortion of the velocity and the sequential deformation of a multiplicity of scales, the proper amount of distortion at each scale is crucial for the appearance of anomalous scaling and the manifestation of the actual intermittency of the dissipative scales. The first two elements are sufficient to produce concentrated velocity gradients, essentially correct cubic statistical moments dependent on velocity gradients and the interrelation between vorticity and strain rate, but the anomalous scaling and intermittency only arise when the proper physical information about the extent of the distortion at each scale is introduced. This information, in the form of the particular (K41) eddy turnover time for each scale, becomes the only input of real turbulence dynamics (in addition to the energy spectrum) that is provided. Note that the prescribed time scale follows standard K41 scaling and does not include *a priori* prescribed intermittency corrections—the intermittency corrections to scaling of structure functions and dissipation arise from the procedure itself.

It is remarkable that with a relatively simple process as the one shown in this paper, many nontrivial features of turbulence can still be reproduced. Per step, the computational cost of the procedure essentially is similar to the cost of DNS, but it has to be performed for only a few such steps. The cost is dominated by the cost of the time stepping at the smallest scale, and so the cost is essentially similar to performing DNS with a number of time steps equal to the ratio D as given in Eq. (17). This ratio scales as the one-third power of the scale ratio between largest and smallest length scales. Hence, when this ratio is of order 10^3, the cost is of order $O(10)$ time steps. This is far less expensive than initializations of DNS that typically require hundreds or thousands of time steps (see Ref. [14] for such a comparison).

It is also worthwhile mentioning that if the time steps are reduced, representations of the viscous effects are included, and the procedure is repeated indefinitely, the method is expected to approach, in some manner, actual DNS. How this approach takes place and how the synthetic fields begin to tend to DNS solutions is left for future inquiries. Also, future work on this topic will include the study of passive scalar fields and passive vectors generated by this approach.

ACKNOWLEDGMENTS

We thank Professor G. Eyink for helpful discussions, specifically for suggesting the use of the turnover time scale. C.R. thanks the support from Project No. USM-DGIP 250806 and from NSF Grant No. CBET-0553314.

[1] R. Benzi, L. Biferale, A. Crisanti, G. Paladin, M. Vergassola, and A. Vulpiani, Physica D **65**, 352 (1993).
[2] A. Arneodo, E. Bacry, and J. Muyz, J. Math. Phys. **39**, 4142 (1998).
[3] J. Eggers and S. Grossmann, Phys. Rev. A **45**, 2360 (1992).
[4] A. Juneja, D. Lathrop, K. Sreenivasan, and G. Stolovitsky, Phys. Rev. E **49**, 5179 (1994).
[5] L. Biferale, G. Boffetta, A. Celani, A. Crisanti, and A. Vulpiani, Phys. Rev. E **57**, R6261 (1998).
[6] A. Scotti and C. Meneveau, Physica D **127**, 198 (1999).

[7] A. Scotti and C. Meneveau, Phys. Rev. Lett. **78**, 867 (1997).
[8] A. Kerstein, W. T. Ashurst, S. Wunsch, and V. Nilsen, J. Fluid Mech. **447**, 85 (2001).
[9] R. McDermott, A. Kerstein, R. Schmidt, and P. J. Smith, J. Turbul. **6**, 1 (2005).
[10] J. C. H. Fung and J. C. Vassilicos, Phys. Rev. E **57**, 1677 (1998).
[11] A. Majda and P. Kramer, Phys. Rep. **314**, 237 (1999).
[12] K. J. Falconer and T. C. O'Neil, Proc. R. Soc. London, Ser. A **452**, 1433 (1996).
[13] P. Kestener and A. Arneodo, Phys. Rev. Lett. **93**, 044501 (2004).
[14] C. Rosales and C. Meneveau, Phys. Fluids **18**, 075104 (2006).
[15] J. Bec and U. Frisch, Phys. Rev. E **61**, 1395 (2000).
[16] U. Frisch, J. Bec, and B. Villone, Physica D **152-153**, 620 (2001).
[17] S. Shandarin and Y. Zeldovich, Rev. Mod. Phys. **61**, 185 (1989).
[18] S. Gurbatov, A. Malakhov, and A. Saichev, *Nonlinear Random Waves and Turbulence in Nondispersive Media: Waves, rays and particles* (Manchester University Press, Manchester, 1991).
[19] G. Falkovich, K. Gawedzki, and M. Vergassola, Rev. Mod. Phys. **73**, 913 (2001).
[20] A. Monin and A. Yaglom, *Statistical Fluid Mechanics: Mechanics of Turbulence* (MIT Press, Cambridge, MA, 1975), Vol. 2.
[21] U. Frisch, *Turbulence: The legacy of A. N. Kolmogorov* (Cambridge University Press, Cambridge, England, 1995).
[22] K. Sreenivasan and R. Antonia, Annu. Rev. Fluid Mech. **29**, 435 (1997).
[23] A. Kolmogorov, J. Fluid Mech. **13**, 82 (1962).
[24] C. Meneveau and K. Sreenivasan, J. Fluid Mech. **224**, 429 (1991).
[25] C. Meneveau and K. R. Sreenivasan, Phys. Rev. Lett. **59**, 1424 (1987).
[26] R. H. Kraichnan, Phys. Rev. Lett. **65**, 575 (1990).
[27] T. Gotoh and R. Kraichnan, Phys. Fluids **5**, 445 (1970).
[28] Y. Li and C. Meneveau, Phys. Rev. Lett. **95**, 164502 (2005).
[29] Y. Li and C. Meneveau, J. Fluid Mech. **558**, 131 (2006).
[30] S. Orzag and G. Patterson, Phys. Rev. Lett. **28**, 76 (1972).
[31] R. Rogallo (unpublished).
[32] S. Pope, *Turbulent Flows* (Cambridge University Press, Cambridge, England, 2000).
[33] H. Tennekes, J. Fluid Mech. **67**, 561 (1975).
[34] F. Anselmet, Y. Gagne, E. Hopfinger, and A. Antonia, J. Fluid Mech. **140**, 63 (1984).
[35] O. Boratav, Phys. Fluids **9**, 1206 (1997).
[36] S. Kurien and K. R. Sreenivasan, Phys. Rev. E **64**, 056302 (2001).
[37] T. Gotoh, D. Fukayama, and T. Nakano, Phys. Fluids **14**, 1065 (2002).
[38] L. Chevillard, B. Castaing, and E. Lévêque, Eur. Phys. J. B **45**, 561 (2005).
[39] L. Chevillard, B. Castaing, E. Lévêque, and A. Arneodo, Physica D **218**, 77 (2006).
[40] Y. Kaneda and T. Ishihara, J. Turbul. **7**, 1 (2006).
[41] A. Tsinober, M. Ortenberg, and L. Shtilman, Phys. Fluids **11**, 2291 (1999).
[42] A. Tsinober, Eur. J. Mech. B/Fluids **17**, 421 (1998).
[43] A. Tsinober, in *Turbulence Structure and Vortex Dynamics*, edited by J. Hunt and J. Vassilicos (Cambridge University Press, Cambridge, England, 2000), pp. 164–191.
[44] N. Cao, S. Chen, and G. Doolen, Phys. Fluids **11**, 2235 (1999).
[45] A. Vincent and M. Meneguzzi, J. Fluid Mech. **258**, 245 (1994).
[46] T. Passot, H. Politano, P. Sulem, J. Angilella, and M. Meneguzzi, J. Fluid Mech. **282**, 313 (1995).
[47] J. Hunt, in *Turbulence Structure and Vortex Dynamics*, edited by J. Hunt and J. Vassilicos (Cambridge University Press, Cambridge, England, 2000), pp. 192–243.
[48] K. Sreenivasan, Annu. Rev. Fluid Mech. **23**, 539 (1991).
[49] B. Mandelbrot, J. Fluid Mech. **62**, 331 (1974).
[50] T. C. Halsey, M. H. Jensen, L. P. Kadanoff, I. Procaccia, and B. I. Shraiman, Phys. Rev. A **33**, 1141 (1986).
[51] K. Sreenivasan and P. Kailasnath, Phys. Fluids A **5**, 512 (1993).
[52] E. Villermaux, B. Sixou, and Y. Gagne, Phys. Fluids **7**, 2008 (1995).
[53] S. Fauve, C. Laroche, and B. Castaing, J. Phys. II **3**, 271 (1993).
[54] P. Abry, S. Fauve, P. Flandrin, and C. Laroche, J. Phys. II **4**, 725 (1994).
[55] A. Pumir, Phys. Fluids **6**, 2071 (1994).
[56] P. Vedula and P. Yeung, Phys. Fluids **11**, 1208 (1999).
[57] T. Gotoh and R. Rogallo, J. Fluid Mech. **396**, 257 (1999).
[58] C. Kalelkar, Phys. Rev. E **73**, 046301 (2006).
[59] Y. Tsuji and T. Ishihara, Phys. Rev. E **68**, 026309 (2003).
[60] M. Holzer and E. Siggia, Phys. Fluids A **5**, 2525 (1993).
[61] T. Ishihara, Y. Kaneda, M. Yokokawa, K. Itakura, and A. Uno, J. Phys. Soc. Jpn. **72**, 983 (2003).
[62] L. Biferale, P. Gualtieri, and F. Toschi, Phys. Fluids **12**, 1836 (2000).
[63] M. Nelkin, Adv. Phys. **43**, 143 (1994).
[64] R. J. Hill and J. M. Wilczak, J. Fluid Mech. **296**, 247 (1995).
[65] M. Nelkin and S. Chen, Phys. Fluids **10**, 2119 (1998).
[66] R. J. Hill and O. N. Boratav, Phys. Rev. E **56**, R2363 (1997).